KSME Journal, Vol. 7, No. 4, pp. 330~348, 1993

The End Point Control for a MMAM Controlled Flexible Manipulator

Yoonsu Nam*

(*Received March 27, 1993*)

For a high bandwidth, accurate end of arm motion control with good disturbance rejection, the Momentum Management Approach to Motion control(MMAM) is proposed. The MMAM is a kind of position control technique that uses inertial forces, applied at or near the end of arm to achieve high bandwidth and accuracy in movement and in the face of force disturbances. To prove the concept of MMAM, the end point control of a flexible manipulator is considered. For this purpose, a flexible beam is mounted on the x-y table, and the MMAM actuator is attached on the top of the flexible beam. A mathematical model is developed for the flexible beam being controlled by the MMAM actuator and slide base DC motor. A system identification method is applied to estimate some system parameters in the model which can not be determined because of the complexity of the mechanism. In order to optimize the result of the position (/velocity) estimation of a beam end point of which movement is monitored by an accelerometer and machine vision, a Kalman filter technique is applied. For the end point control of the flexible beam, the optimal linear output feedback control is applied.

Key Words: MMAM(Momentum Management Approach to Motion Control), Flexible Manipulator, Proof Mass, System Identification, Accelerometer, Vision System, Kalman Filter, Optimal Linear Output Feedback

1. Introduction

Lightweight manipulators suffer because they are unable to attain high bandwidth position control, or to maintain position in the face of high bandwidth disturbing forces. This is inherent in any manipulator where the driving actuator is separated from the end of arm by a structure which deflects significantly during the motion.

Alternate approaches to resolving these problems are, (1) augmenting the arm with additional fine motion device (micro-manipulator) on the end-effector to achieve high positional accuracy and variable compliance without moving the entire structure (Sharon and Hardt, 1984 ; Hollis, 1987), (2) active control of the flexible modes of the structure to reduce the effects of deflections by using a control algorithm that specifically accounts for the deflections (Cannon and Schmitz, 1984 ; Kanoh and Lee, 1985 ; Hasting and Book, 1985), (3) bracing against some object near the end-effector to enhance accuracy and to bear the interaction force between the end-effector and the environment (Book and Sangveraphunsiri, 1984), (4) more efficient structures which achieve better performance per unit weight by using (a) stiffer materials, (b) more efficient geometries, e.g. closed chains, or (c) passive damping (Albert, 1986), (5) momentum management approach to motion control(MMAM) which uses momentum exchange between the manipulator end of arm and one or more proof-mass(es) near the tip of a manipulator (Dickerson and Nam, 1988 ; Nam, 1991).

The approach using micro-manipulators is excellent where rapid positioning of very light payloads is required. If the payload is heavy, the forces required to move the payload rapidly are

* Flight Dynamics & Control Div. (3-1-6), Agency for Defense Development, P.O. Box 35, Yusung, Taejon 305-600, Korea

such that a motion of the micro-manipulator results more in bending and vibration of the arm than motion of the payload. Similarly, if there are high bandwidth disturbing forces, these are transmitted to the arm. A way of countering that, a bracing strategy, has been suggested which may be quite practical when there is a convenient place to brace.

A momentum management approach to the motion control(MMAM) has been suggested for overcoming this shortcoming. MMAM refers to momentum exchange between the manipulator end of arm and one or more proof mass(es) near the tip of a manipulator. External disturbance force on the end effector is temporally transferred to the proof mass(es) in order to maintain the end point desired position. This momentum is subsequently absorbed by the manipulator structure through the proper control of the main servo system. Momentum management has also been used in space applications to control the attitude of a space craft (Ham and Greeley, 1987). The use of MMAM to control the position of a robot, machine tool, or conventional motion control system does not seem to have been addressed earlier.

2. Description of Experimental Setup

Figure 1 shows the schematic of the experimental setup and MMAM device. A flexible beam is clamped on the slide base of x-y table. The flexible beam, which has the length of 28.5 inches, the thickness of 1/8 inches, and the width of 1.5 inches, is made of aluminum. The table is driven by two identical DC motors, and has a chain

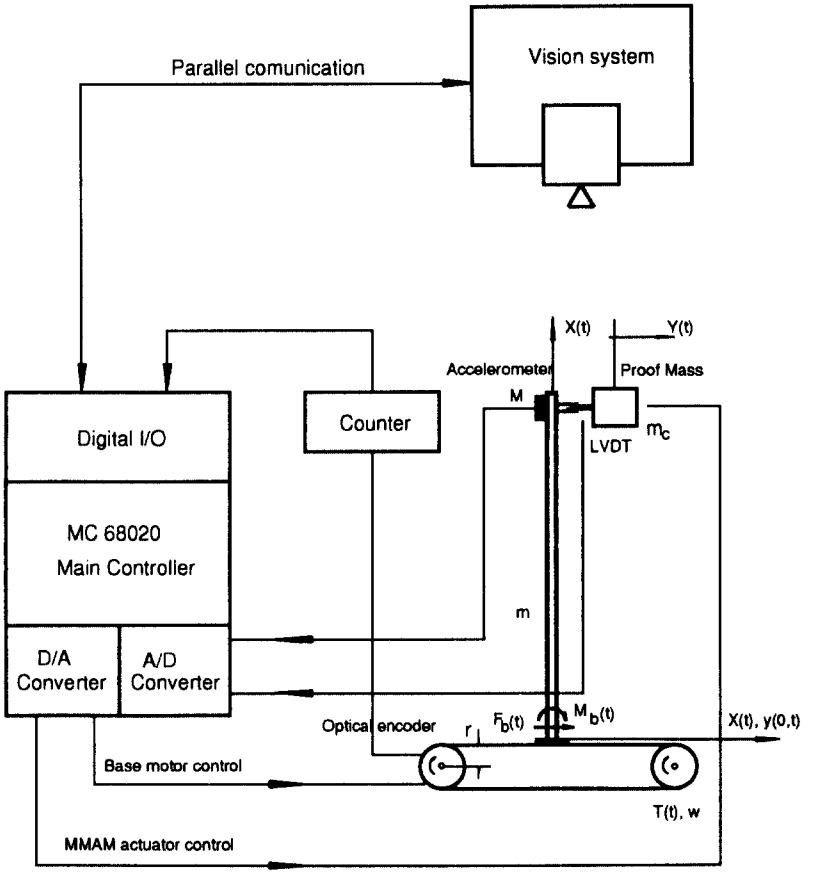

Fig. 1 Experimental setup

mechanism to position the slide base. These DC motors are separately located at both ends of the chain drive as shown in Fig. 1. Each DC motor has a gear box with the reduction ratio of 65.5 : 1.

On the top of a beam, the MMAM device is mounted (refer a detailed plot of the beam end point in Fig. 8). The MMAM device is composed of a coil and permanent magnet (called proof mass). This coil is fixed on the beam so that the generated magnetic force could be transferred to an end point of a beam directly, and the permanent magnet is attached through a flexure spring to the beam. The DC motor of the x-y table and the MMAM device are each driven by a current control type linear bipolar amplifier.

An optical encoder attached on the DC motor axis is used for the measurement of the slide base displacement. The acceleration and position of the end point of the flexible beam are sensed by an accelerometer and machine vision. To measure the relative displacement between the flexible beam end point and the proof mass, an LVDT is used.

The main controller, MC68020, monitors the system status, and generates the proper control signals to the system. The control software, which is written as the MC68020 assembly language makes communication with the external devices such as a vision system, optical encoder, accelerometer, LVDT, and current amplifiers through digital I/O, A/D and D/A converters. It also has an optimal full state observer inside. All the arithmetic operations are performed using the floating point coprocessor, MC68881. The host computer, IBM-PC is used for communication with the main controller MC68020. It downloads the control software to, and uploads experimental data from the main controller under the QUICK BASIC environment through a serial communication.

3. Mathematical Modeling

The Euler-Bernoulli beam model, in which shear deformation and rotary inertia effects are ignored, is used for the flexible beam. Then, the motion of a flexible beam is governed by the equation of

$$m\frac{\partial^2 y(x,\ t)}{\partial t^2}+EI\frac{\partial^4 y(x,\ t)}{\partial x^4}=0, \tag{1}$$

with the boundary condition of

$$y(0,\ t)=0,$$
$$\frac{\partial y}{\partial x}(0,\ t)=0,$$
$$\frac{\partial^2 y}{\partial x^2}(L,\ t)=0,$$
$$M\frac{\partial^2 y}{\partial t^2}(L,\ t)=-\left\{-EI\frac{\partial^3 y}{\partial x^3}(L,\ t)\right\}, \tag{2}$$

where m=mass per unit length of beam,
M=concentrated mass on the top of beam,
L=length of the beam.

The solution of Eq. (1) is given as

$$y(x,\ t)=\sum_{i=1}^{\infty}\phi_i(x)q_i(t), \tag{3}$$

where $q_i(t)=i$-th generalized coordinate,

$$\phi_i(x)=c_i\{\sin\beta_i x-\sinh\beta_i x-\gamma_i(\cos\beta_i x-\cosh\beta_i x)\},$$
$$\gamma_i=\frac{\sin\beta_i L+\sinh\beta_i L}{\cos\beta_i L+\cosh\beta_i L}, \tag{4}$$

By the boundary conditions of Eq. (2), each β_i has to meet the frequency equation of (Meirovitch, 1986)

$$\frac{M}{m}\beta(\cos\beta L\sinh\beta L-\sin\beta L\cosh\beta L)+1+\cos\beta L\cosh\beta L=0. \tag{5}$$

By using the orthonormality condition of

$$m\int_0^L\phi_i(x)\phi_j(x)dx+M\phi_i(L)\phi_j(L)=\delta_{ij}, \tag{6}$$

and considering the exciting force terms by the MMAM device and the movement of slide base, the generalized coordinate $q_i(t)$ must satisfy the following equation of

$$\ddot{q}_i(t)+\omega_i^2 q_i(t)=\phi_i(L)f(t)-\frac{d^2X}{dt^2}\left\{m\int_0^L\phi_i(x)dx+M\phi_i(L)\right\}, \tag{7}$$

where $f(t)$ is the generated force by MMAM $\frac{d^2X}{dt^2}$ is the acceleration of the slide base.

It is generally sufficient to approximate the end point displacement $y(L,\ t)$ by including only 2 or

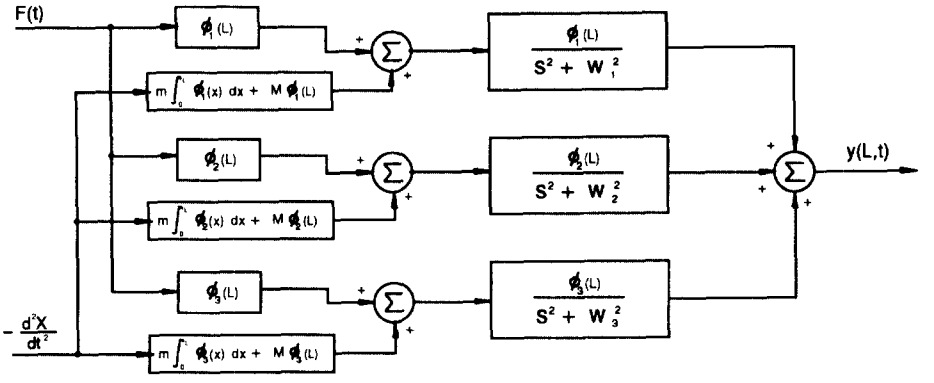

Fig. 2 Block diagram of beam dynamics

3 terms in Eq. (3)

$$y(L,\ t)=\sum_{i=1}^{2(\text{or}3)}\phi_i(L)q_i(t). \tag{8}$$

Figure 2 is the block diagram representation of Eqs. (7) and (8).

3.1 The effect of MMAM actuator

The block diagram of Fig. 3 shows the dynamics of a beam end point, $y(L,\ t)$, and the proof mass displacement, $Y(t)$, for the input voltage to the coil of MMAM actuator. The inner loops represent the flexure spring force, and damping effect, and outer loop is caused by the back EMF of the MMAM actuator. The system parameters of Fig. 3 are listed on Table 1. Some system parameters are measured directly, and others (superscripted with $*$ in Table 1) are determined by the system identification method explained in the next section. The transfer function of the acceleration, $\ddot{y}(L,\ t)$ from the input voltage, V_m, is given by

$$\frac{\ddot{y}(L,\ t)}{V_m}=\frac{-C_1\dfrac{K_{t1}}{R_1}q(s)s^2}{p(s)\left\{s^2+\dfrac{C_1}{m_c}\left(\dfrac{K_{t1}K_{e1}}{R_1}+B_1\right)s+\dfrac{C_1K_1}{m_c}\right\}+C_1q(s)\left\{\left(\dfrac{K_{t1}K_{e1}}{R_1}+B_1\right)s+K_1\right\}}, \tag{9}$$

where

$$\frac{q(s)}{p(s)}=\sum_{i=1}^{3}\frac{\phi_i^2(L)s^2}{s^2+\omega_i^2}.$$

Figure 4 is bode plot of the transfer function of Eq. (9). There are four peaks. The second peak is caused by the resonance of the MMAM actuator (i.e. by the flexure spring and proof mass). The remaining peaks are from 3 modal frequencies of

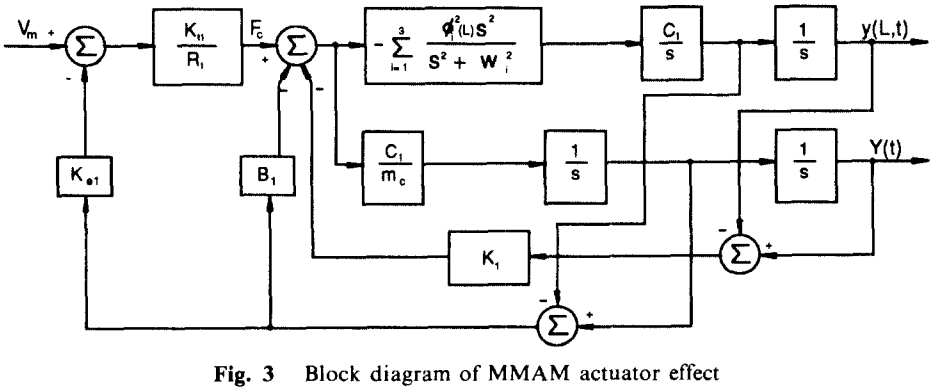

Fig. 3 Block diagram of MMAM actuator effect

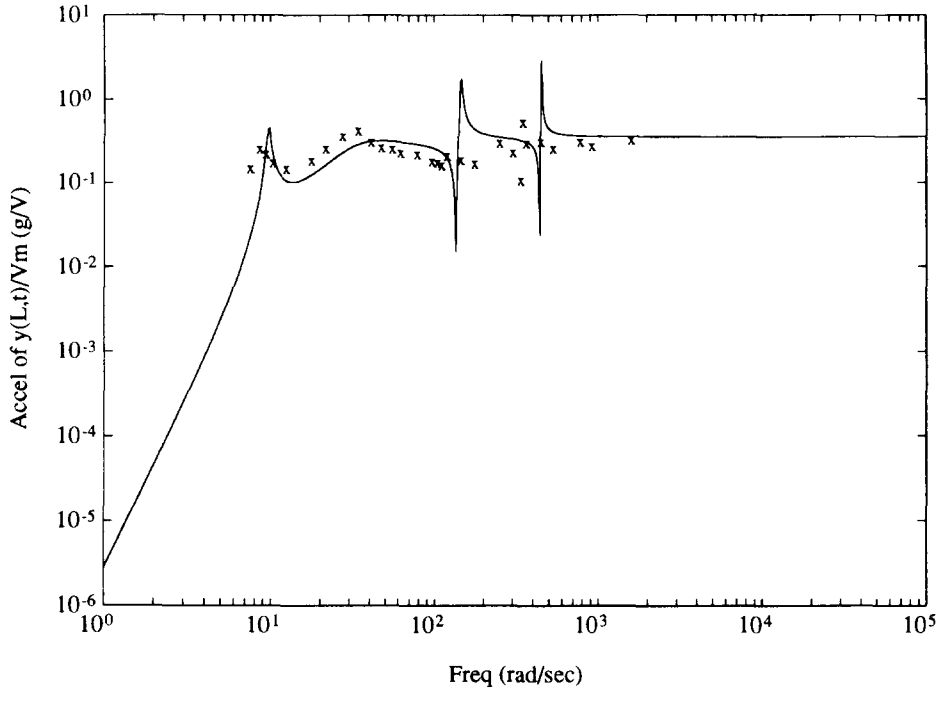

Fig. 4 Frequency response of the end point acceleration for V_m

the beam. The point designated by 'x' is the measured acceleration of a beam end point for the input voltage to the MMAM actuator at each exciting frequency. The discrepancy between the analytic and experimental results becomes larger for the high modal frequencies. One of the reasons of this difference comes from the mounting mechanism of the system on the aluminum base plate. Figure 4 shows the experimental data match well with the analytical results up to the second modal frequency.

3.2 The effect of the movement of slide base

As shown in Fig. 1, the flexible beam is clamped on the slide base. Therefore, the shear force, $F_b(t)$, and bending moment, $M_b(t)$, at a clamping point caused by a beam deflection must be considered on the dynamics of the slide base. The differential equation for a motor rotation is given by

$$J\dot{\omega}(t)+B_2\omega(t)=T(t)+\frac{1}{N}\{M_b(t)+rF_b(t)\}, \quad (10)$$

where

$$M_b(t)=EI\sum_{i=1}^{n}\phi_i''(0)q_i(t),$$
$$F_b(t)=-EI\sum\phi_i'''(0)q_i(t),$$

and J is total moment of inertia on the motor axis, N is gear reduction ratio, and $T(t)$ is the developed torque by the motor.

By combining Eqs. (7), (10) and DC motor characteristic, the block diagram of Fig. 5 is constructed. The system parameters in Fig. 5 are shown on Table 2. Again, some parameters superscripted with $*$ in Table 2 are found from the parameter identification method. The resulting transfer function of the slide base displacement, X, and the end point acceleration, $\ddot{y}(L, t)$, from the input voltage of the DC motor is given by

$$\frac{X}{V_b}=\frac{C_2\frac{K_{t2}}{R_2}p_1(s)}{sp_1(s)(Js+C_2B_2+\frac{K_{t2}K_{e2}}{R_2})+C_2C_3s^2q_1(s)}, \quad (11)$$

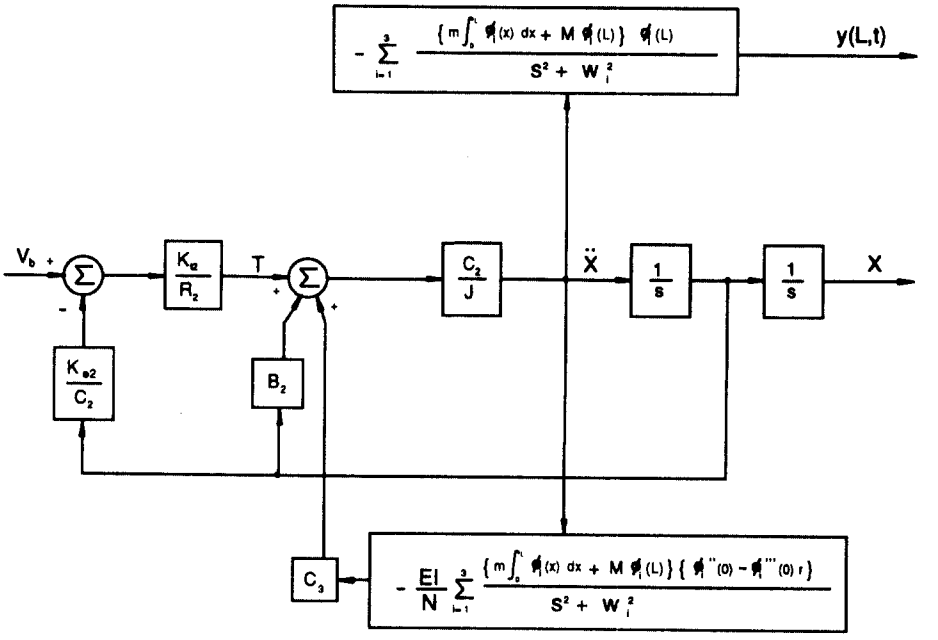

Fig. 5 Block diagram of slide base dynamics

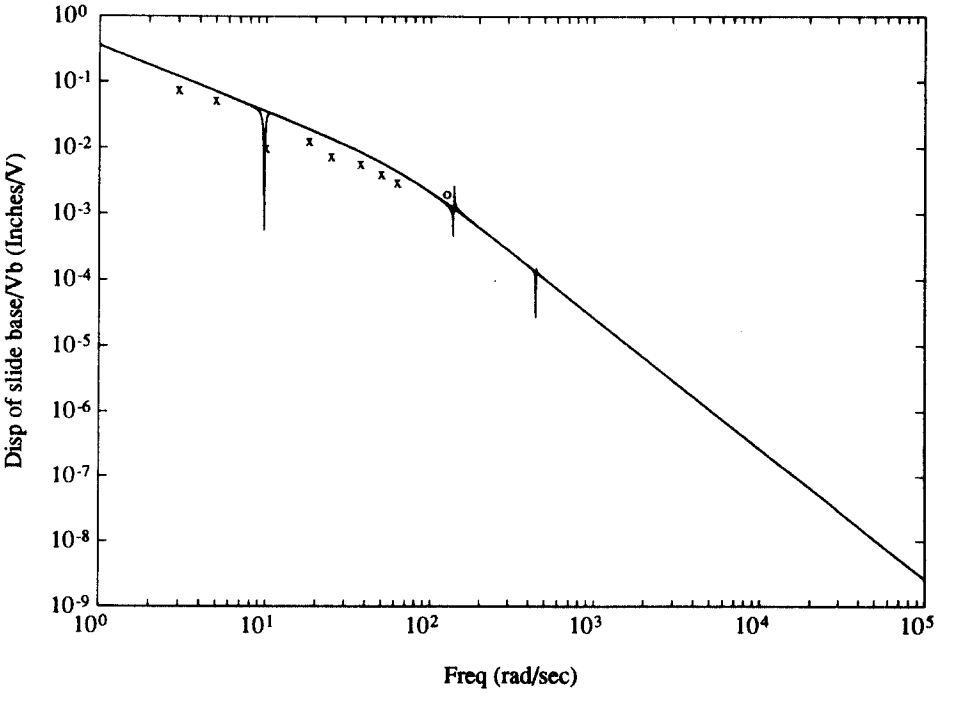

Fig. 6 Frequency response of slide base displacement for V_b

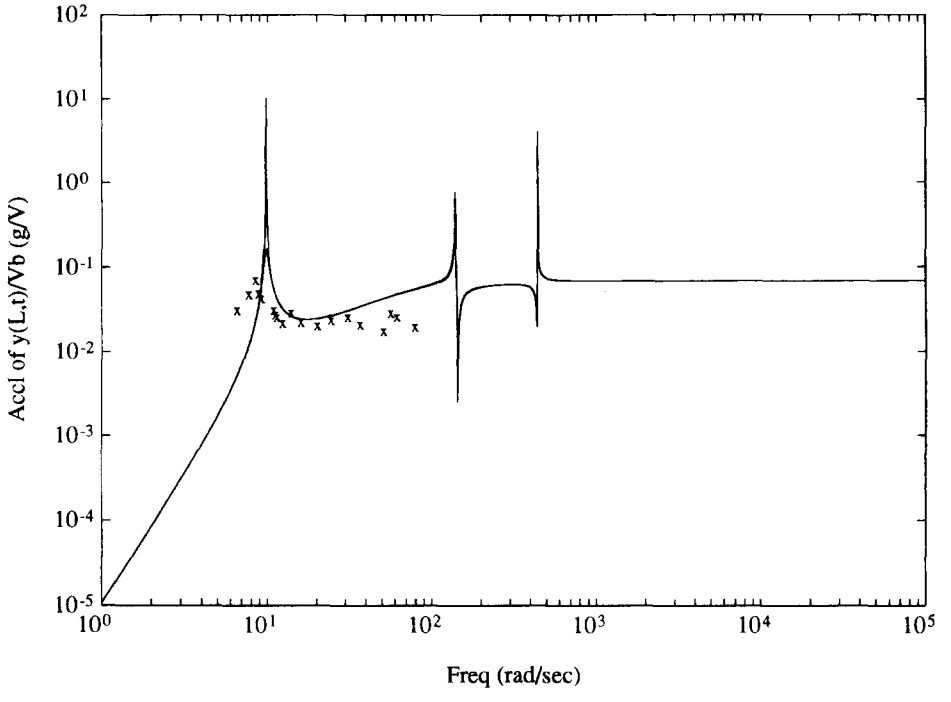

Fig. 7 Frequency response of the end point acceleration for V_b

$$\frac{\ddot{y}(L,\ t)}{V_b}=\frac{C_2\frac{K_{t2}}{R_2}sp_1(s)q_2(s)}{p_1(s)p_2(s)(Js+C_2B_2+\frac{K_{t2}K_{e2}}{R_2})+C_2C_3sq_1(s)p_2(s)} \tag{12}$$

where

$$\frac{q_1(s)}{p_1(s)}=\frac{EI}{N}\sum_{i=1}^{3}\frac{\{\phi_i''(0)-\phi_i'''(0)r\}\left\{m\int_0^L\phi_i(x)dx\right\}}{s^2+\omega_i^2},$$

$$\frac{q_2(s)}{p_2(s)}=\sum_{i=1}^{3}\frac{\phi_i(L)\left\{m\int_0^L\phi_i(x)dx\right\}}{s^2+\omega_i^2},$$

Figure 6 is the Bode plot for Eq. (11). The solid line in Fig. 6 represents the Bode plot of this transfer function, and dashed line the Bode plot of the same transfer function, when the influence of the beam deflection forces (i.e. $F_b(t)$ and $M_b(t)$) are ignored. The points 'x' are the measured displacement of the slide base. Based on the experimental observation, there is no response of the slide base beyond 20 Hz of the driving signal, even though the maximum input voltage(10 V) was applied to the DC motor.

The Bode plot of the transfer function of the end point acceleration, $\ddot{y}(L,\ t)$, for the base DC motor driving voltage, V_b, is shown as solid line in Fig. 7. Again, the dotted line represents the same transfer function, when the effect of a flexible beam deflection on the dynamics of the slide base is ignored. The measured end point acceleration is also shown as the mark 'x'. Because of the dead response of the slide base for the driving signals above 20 Hz due to the backlash, the second and third mode frequency could not be measured.

4. System Parameter Identification

The modeling of a flexible beam dynamics is completed mathematically. Some system parameters such as the mass of the permanent magnet(m_c), the resistance of the coil (R_1)... can be easily measured, but others such as a flexure spring constant (K), force constant (K_{t1}) of the MMAM actuator... can not. By collecting the

system input-output data, and using the system identification method such as the least square method like an ARX, ARMAX, OE model (Ljung, 1987), those unknown system parameters in the MMAM actuator and slide base moving mechanism are estimated.

Ideally, the impulse function, which has a flat power spectrum, is the best input signal for the system identification, because the system is excited by a wide spectrum of frequencies. But, one of the practical optimum input signal is the so-called pseudo-random binary sequence(PRBS) (Ljung, 1987), which is a band-limited white noise sequence.

4.1 Identification of the MMAM actuator

The MMAM actuator, which is schematically described in Fig. 8, can be modelled as

$$\frac{Y(s)}{V_m(s)}=\frac{\frac{C_1K_{t1}}{R_1m_c}}{s^2+(\frac{K_{t1}K_{e1}}{R_1}+B_1)\frac{C_1}{m_c}s+\frac{C_1K_1}{m_c}}. \tag{20}$$

Again, the meaning of each system parameter is given on Table 1. If we use the z-transform representation, Eq. (20) is changed to

$$\frac{Y(z)}{V_m(z)}=\frac{b_1z^{-1}+b_2z^{-2}}{1+a_1z^{-1}+a_2z^{-2}}. \tag{21}$$

The numerical values of the coefficients in Eq. (21) depend on the sampling time interval.

As mentioned before, the system parameters in Eq. (20) except the mass of a permanent magnet (m_c), and the resistance of a coil(R_1) can not be easily measured. But, by using the system identification method, the coefficients in Eq. (21)

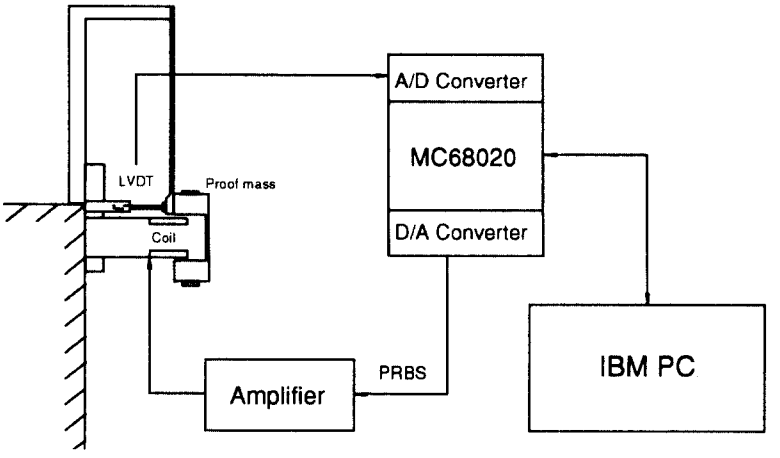

Fig. 8 Experimental setup for identification of MMAM

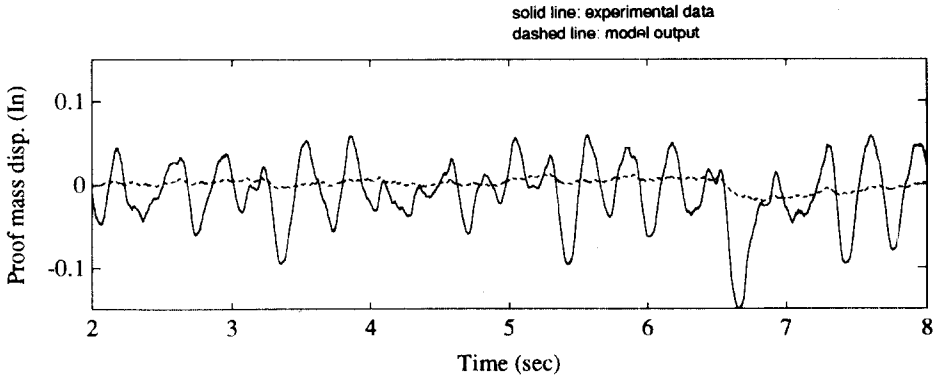

Fig. 9 ARX model evaluation for MMAM actuator

can be estimated. Then, by converting this estimated z-transform into the laplace transform, and matching the coefficients of this converted (i.e. estimated) z-transform with that of Eq. (20), these unknown system parameters can be determined.

The experimental setup is depicted in Fig. 8. The PRBS, which has the alternating magnitude of -1.0 V and 1.0 V excites the MMAM actuator. The disturbed proof mass displacement is measured using LVDT, and recorded on the RAM of MC68020 microcomputer. The sampling time of this experiment is 2 msec. The experimental data

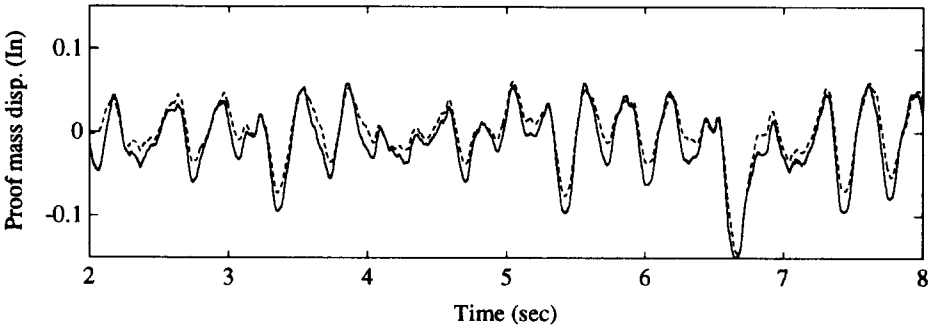

Fig. 10 ARMAX model evaluation for MMAM actuator

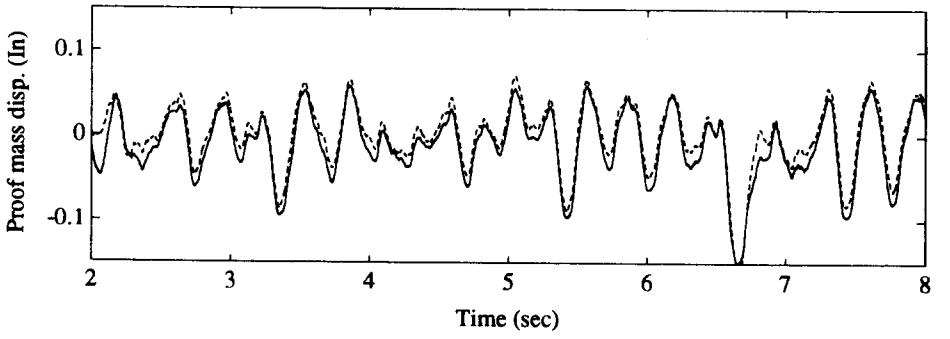

Fig. 11 OE model evaluation for MMAM actuator

Table 1 System parameters in Fig. 3

System parameter	Description	Value	Unit
R_l	Resistance of coil	4	ohm
K_{el}*	Back EMF constant	0.061441	V/(in/sec)
K_{tl}*	Force constant	0.54376	lb_f/A
K_l*	Flexure spring constant	0.68771	lb_f/inches
B_l*	Damping constant	1.8082×1^{-2}	lb_f/(in/sec)
m_c	Mass of permanent magnet	0.6614	lb_m
C_l	Conversion factor	386.4	$(in/sec^2)/g$
L	Length of beam	29	inches
m	Mass/unit length of beam	1.8338×10^{-2}	lb_m/inches
M	Concentrated mass	0.4852	lb_m

are sampled during 8 seconds. These input-output data are uploaded to the IBM-PC for the analysis. The MATLAB system identification software package is used for the manipulation of these data.

Among the uploaded experimental input-output data, the first 1000 data points, which amount to the data of the first 2 seconds, are selected for building a model. The remaining data are used in testing the accuracy of the model. A simple model evaluation is done by running a simulation that real input data are fed into the model, and comparing the simulated output with the actual, measured output. Figures 9, 10 and 11 represent this result of the model evaluation for the parametric model of ARX, ARMAX, and OE

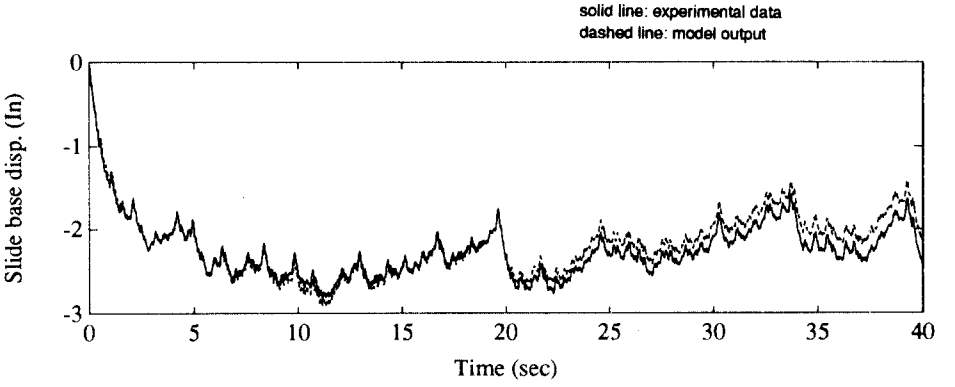

Fig. 12 ARX model evaluation for slide base mechanism

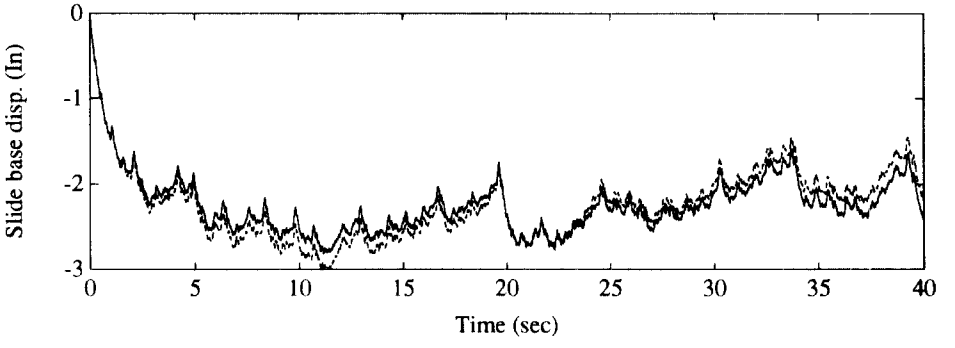

Fig. 13 ARMAX model evaluation for slide base mechanism

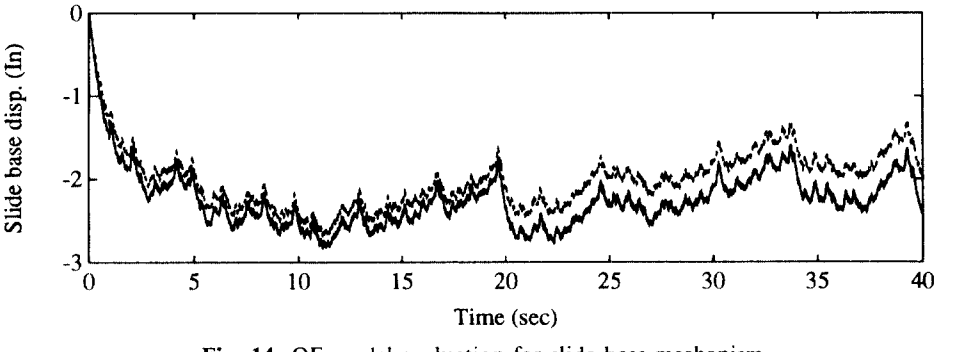

Fig. 14 OE model evaluation for slide base mechanism

Table 2 System parameters in Fig. 5

System parameter	Description	Value	Unit
R_2	Resistance	8.2	ohm
K_{e2}	Back EMF constant	0.0388	V/(r/sec)
K_{t2}	Torque constant	0.50	$oz_f in/in/sec$
r	Radius of chain	1.5	inches
I	Area moment of inertia	2.4414×1^{-4}	in^4
E	Young's modulus of Al	10.5×10^6	lb_f/in^2
N	Reduction ratio	76.4385	-
J*	Moment of inertia	9.5206×10^{-4}	$oz_f ins^2$
C_2	Conversion factor	1.8571×10^{-2}	in/rad
C_3	Conversion factor	16	lb_f/oz_f

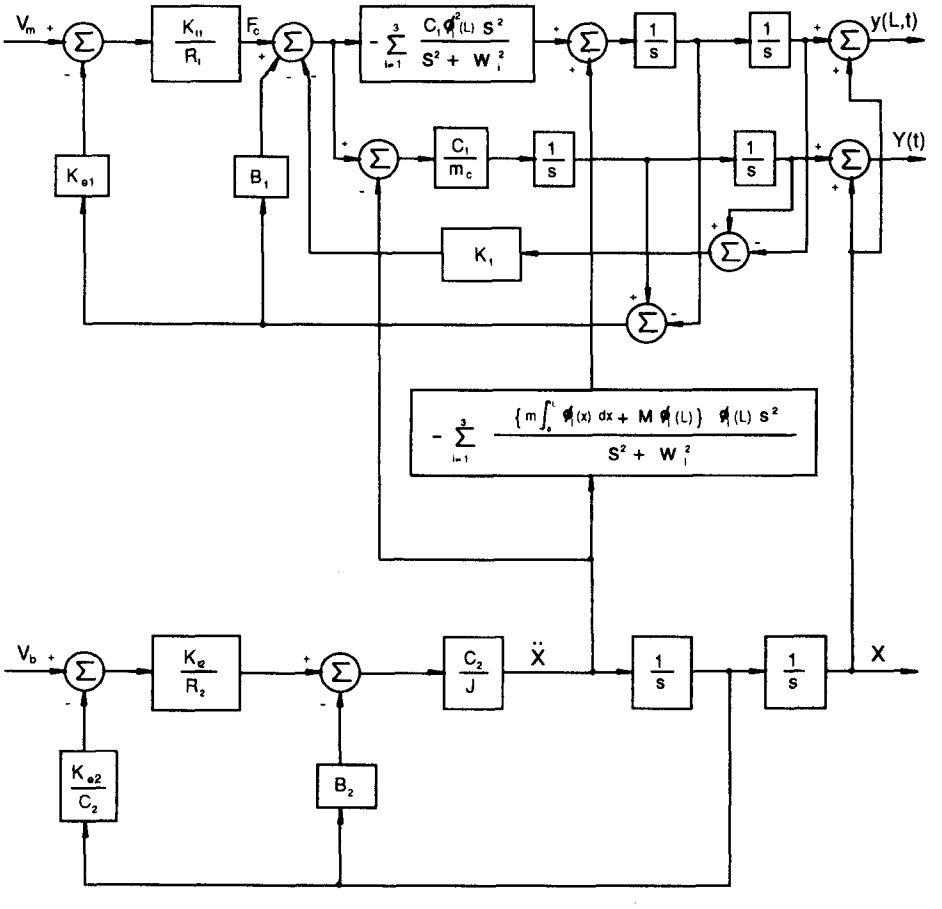

Fig. 15 Block diagram of simplified model

for the time interval from 2 to 8 seconds. The initial discrepancies between the experimental data and the model output in these figures are due to the transient responses of the each model due to the wrong initial conditions of the model. As shown clearly in Fig. 9, the identification result of the ARX model is the worst among the three models. The OE model of Fig. 11 is slightly better than the ARMAX model of Fig. 10 in reproducing the experimental data. Therefore, the OE model is chosen in identifying the coefficients in Eq. (21). Again, these coefficients are used for the determination of the system parameters in Eq. (20). Those numerical values are shown on Table 1.

4.2 Identification of the slide base mechanism

The same procedures as that of identifying the MMAM actuator dynamics were taken for the slide base moving mechanism. Therefore, only the experimental data are described here. Figures 12, 13 and 14 show the results of the model output of ARX, ARMAX, and OE with the actual response of the slide base. As shown in Fig. 12, the ARX model output gives the best fit to the experimental data among the three models. Therefore, the system parameters of the slide base mechanism were determined based on the ARX model. The numerical values of these parameters are shown on Table 2.

In conclusion, the modeling of the whole system can be described by the block diagram of Fig. 15. To evaluate the accuracy of the model, several experiment are made. It is shown in the Figs. 4, 6 and 7 that these experimental data match well with the analytic results.

5. A Measurement of the End Point Movement

Accurate, high bandwidth measurement of position is essential to quality performance of a feedback position control system. In many cases it is not convenient to make such measurements with direct contact sensors, for example, in the case of the end point of a flexible beam. In these situations machine vision can be used. The sampling rate in machine vision is restricted by video image processing time, and the errors in such measurements may not be acceptable. The use of an inertial measurement between vision samples can be used to reduce both of these difficulties. The use of an accelerometer attached to the beam end point is used to supplement the vision measurements to arrive at a higher bandwidth and more accurate position estimator. In this paper, the end point displacement of a flexible beam is estimated by using a piezoresistive type accelerometer and landmark tracking system(LTS). The LTS is a grey-scale industrial vision system using pinhole imaging (Lee and Dickerson, 1990). A Kalman filter algorithm for minimizing the effects of random errors in both sensor outputs on the position estimate is developed.

5.1 Application of KALMAN filter to position estimation

Consider now an one dimensional dynamic system in Fig. 16 used to estimate the position of an object based on the output of an accelerometer and a vision system. If we assume T and T_v be the sample time intervals for the accelerometer and vision system respectively, where there is an integer N such that $T_v=NT$, then the discrete state representation of such a dynamic system is described as

$$x_{k+1}=\begin{bmatrix}1 & T\\ 0 & 1\end{bmatrix}x_k+\begin{bmatrix}T^2/2\\ T\end{bmatrix}(u_k+w_k), \quad (22)$$

where

$x_k=[y_k \ \dot{y}_k]^T$ at $t=kT$,
y_k=actual position,
z_k=measured position,
u_k=measured acceleration,

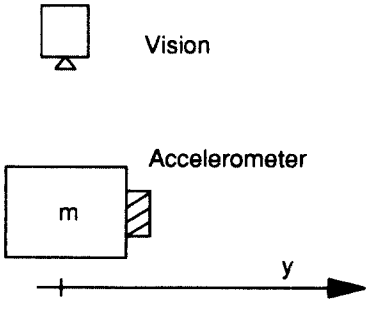

Fig. 16 One dimensional dynamic system

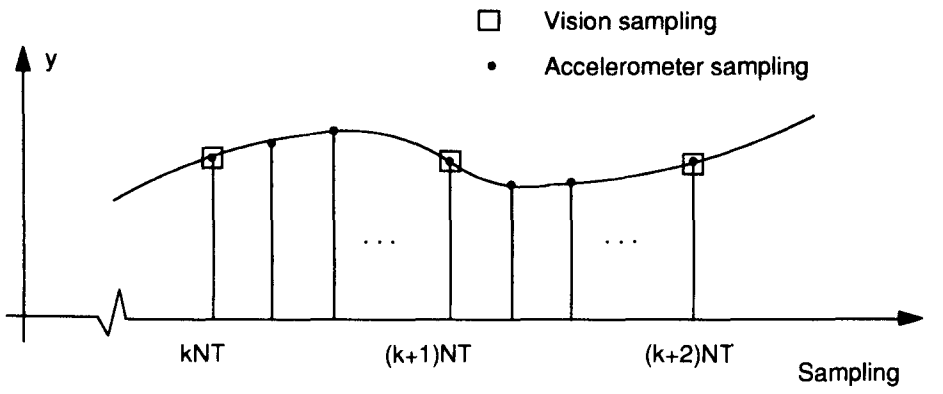

Fig. 17 Sampling of vision and accelerometer data

w_k=error in acceleration measurement,
v_k=error in position measurement.

It will be assumed that the error is "white noise," which means that the subsequent analysis considers errors caused only by random effects, and not the effects of dynamics, or any other systematic errors in the sensors.

This sampling procedure is described in Fig. 17. Because a vision measurement is available only at every T_v second, the measurement equation is given as

$$z_{(k+1)N}=[1\ \ 0]x_{(k+1)N}+v_{(k+1)N},$$
$$=Hx_{(k+1)N}+v_{(k+1)N}. \tag{23}$$

During the interval $[kNT, (k+1)NT)$, during which time no vision measurement made, the estimate of state x, and error covariance P grows according to (Gelb, 1974)

$$\hat{x}_{(k+1)}=F\hat{x}_k+Gu_k,$$
$$P_{k+1}=FP_kF^T+GR_wG^T, \tag{24}$$

where

$\hat{x}_k$=estimate of the state at $t=kT$,
$R_w=E\{ww^T\}$,

$$P_k=E\{(x_k-\hat{x}_k)(x_k-\hat{x}_k)^T\}=\begin{bmatrix}P_{yk} & P_{yvk}\\ P_{yvk} & P_{vk}\end{bmatrix}.$$

After some matrix manipulations, the relationship between the initial value of $F_{(k+1)N}$(at NT, or T_v, i, e. error covariance matrix just before the vision measurement at $t=(k+1)NT$) is given by

$$P^-_{y(k+1)N}=a_1R_w+P_{ykN}+2NTP_{yvkN}+N^2T^2P_{vkN},$$
$$P^-_{yv(k+1)N}=a_2R_w+P_{yvkN}+NTP_{vkN},$$
$$P^-_{v(k+1)N}=a_3R_w+P_{vkN}, \tag{25}$$

where

$a_1=N^3T^4/3-NT^4/12$,
$a_2=N^2T^3/2$,
$a_3=NT^2$.

When a vision measurement is available, the estimate of state, is modified by the measurement update equation

$$\hat{x}_{(k+1)N}=\hat{x}^-_{(k+1)N}+L_{(k+1)N}\{z_{(k+1)N}-H\hat{x}^-_{(k+1)N}\}, \tag{26}$$

where

$$L_{(k+1)N}=P^-_{(k+1)N}H^T\{HP^-_{(k+1)N}H^T+R_v\}^{-1}. \tag{27}$$

And error covariance matrix P is updated by

$$P_{(k+1)N}=\{I-L_{(k+1)N}H\}P^-_{(k+1)N}, \tag{28}$$

where

$R_v=E\{vv^T\}$,
$L_{(k+1)N}$=Kalman filter gain.

The optimal estimation algorithm characterized by Eqs. (24), (26) and (27) is coded on the main controller in Fig. 1 for measuring the end point movement and its velocity (Nam, 1991).

6. Experiment-Disturbance Rejection

For the experimental setup described in Fig. 1, an impulse force is applied on the beam end point. The impulse force is generated by striking a steel ball on the beam end point. To minimize the effect of an impulse force on the end point

displacement, the optimal linear output feedback is used. For the reconstruction of the state vector from the measured variables, a full state observer is applied.

By the simulation of the impulse force excitation of the flexible beam being designed, the contribution of the third mode to the end point displacement is only 0.14459% compared to that of the first. Therefore, the higher mode contributions except the first two modes can be neglected. As discussed in the section of mathematical modeling, there are two control inputs for the end point control. One is by the movement of the slide base(V_b) which is effective in a low frequency region, and the other is by the MMAM actuator(V_m) which has the high bandwidth control capability. By combining acceleration, and machine vision measurement of the flexible beam end point with the KALMAN FILTER algorithm developed in the previous section, we can recover the displacement(y) and velocity ($\dot{y}$) of the beam end point with the accuracy and high bandwidth. The relative displacement(Y-y) of the proof mass to the beam end point is measured using an LVDT installed between the flexible beam and the proof mass. The movement(X) of the slide base can be estimated from the optical encoder attached to the driving DC motor. Therefore, there are four outputs. The discrete-time state space representation of the flexible beam dynamics shown in Fig. 15 by retaining the first two modes is given by the following

$$\begin{aligned} \underline{x}_o(k+1) &= A_o\underline{x}_o(k)+B_o\underline{u}(k), \\ \underline{y}(k) &= C\underline{x}_o(k), \end{aligned} \tag{29}$$

where

$$\begin{aligned} &\underline{x}_o(k)=[x_{o1}(k)\cdots x_{o8}(k)]^T, \\ &\underline{y}(k)=[y(k)\,\dot{y}(k)\,Y(k)-y(k)X(k)]^T, \\ &\underline{u}(k)=[V_m(k)\,V_b(k)]^T, \\ &A_o=\text{system matrix } (8\times 8), \\ &B_o=\text{input matrix } (8\times 2), \\ &C=\text{output matrix } (4\times 8). \end{aligned}$$

The feedback control law of $\underline{u}(k)=-K\underline{x}_o(k)$ for the dynamic system of Eq. (29) is determined by minimizing the following quadratic performance index of

$$PI=\sum_{i=0}^{\infty}\{\underline{x}_o(k)^TQ_o\underline{x}_o(k)+\underline{u}(k)^TR\underline{u}(k)\}. \tag{30}$$

The steady state feedback gain K is given as

$$K=(R+B_o^TSB_o)^{-1}B_o{}^TSA_o, \tag{31}$$

where S is the solution of the following discrete-time version matrix RICCATI equation of

$$0=S-A_o^TSA_o+A_o^TSB_o(R+B_o^T)^{-1}B_oS^TA_o-Q_o. \tag{32}$$

The performance of the optimal linear state feedback system depends on the choice of weighting matrix Q_o for the state variables and R for the inputs. However, there is no systematic way to select these matrices, except for iteratively changing the values of the matrices with some intuitions of a designer to reach at a satisfactory result. After a lot of simulations, the following performance index was chosen.

$$\begin{aligned} PI &= \sum_{k=0}^{\infty}\{\underline{y}(k)^TQ\underline{y}(k)+\underline{u}(k)^TR\underline{u}(k)\}, \\ &= \sum_{k=0}^{\infty}\{q_1y(k)^2+q_2[\,Y(k)-y(k)]^2+q_3\dot{y}(k)^2 \\ &\quad + r_1V_m(k)^2+r_2V_b(k)^2\}. \end{aligned} \tag{33}$$

In Eq. (33), $y(k)$, $\dot{y}(k)$, $Y(k)$, $V_b(k)$, and $V_m(k)$ represents the displacement of the beam end point, its velocity, displacement of the proof mass, and control inputs for the base DC motor and MMAM actuator respectively.

6.1 Experiment using base motor only

Figure 18(a) through Fig. 18(c) display the responses of the beam end point displacement, velocity, and slide base movement for the value of $q_1=1$, $q_2=0$, $q_3=1$, and $R=10^{-3}$ in the performance index of Eq. (33). Because of the nonlinearities in the base slide mechanism such as a stiction and dead zone, the beam end point does not return to the position it had before the impact. The effect of the nonlinearities on the slide base response can be noticed well in Fig. 18(c). The flat response in Fig. 18(c) between 1 second and 2 second is considered as the result of the stiction in the slide base mechanism, and the dead response after 3 second of the dead zone. The mark 'x' in Fig. 18(a) represents a vision data from the machine vision. The sudden rise and drop in the position and velocity estimation signals were the

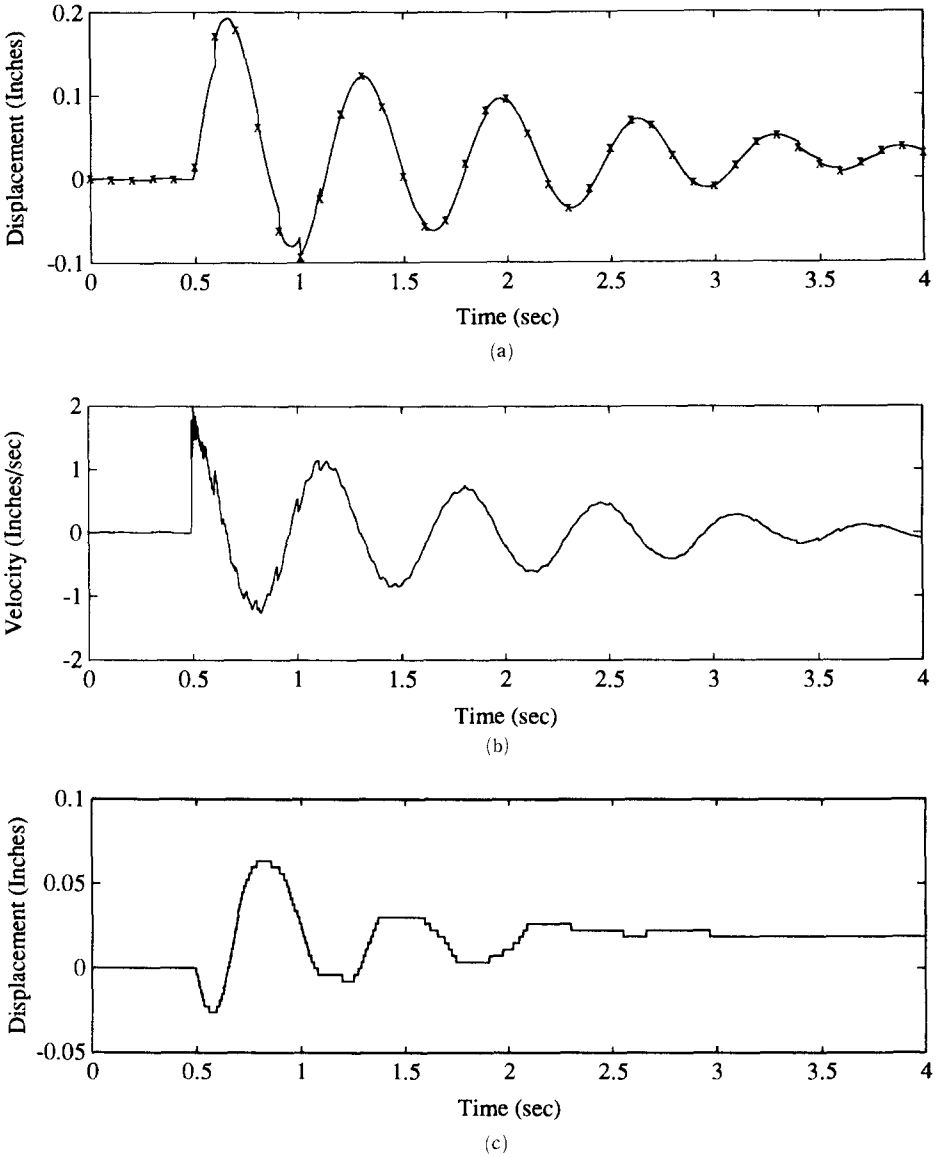

Fig. 18 (a) End point displacement ($q_1=q_3=1$, $q_2=0$, & R=1.0e-3)
(b) End point velocity ($q_1=q_3=1$, $q_2=0$, & R=1.0e-3)
(c)Slide base displacement ($q_1=q_3=1$, $q_2=0$, & R=1.0e-3)

results from a correction by the Kalman filter.

In order to eliminate the steady state error in Fig. 18(a), integral control is added. By augmenting the state x_{o9}[1)] in Eq. (29), which is the integral of y (beam end point), and defined as

$$\dot{x}_{o9}=\phi_1(L)x_{o1}+\phi_2(L)x_{o3}+x_{o7}, \tag{34}$$

and with the additional term of $q_4(x_{o9})$[1)] to the PI of Eq. (33), integral control can be achieved.

Figure 19(a) through Fig. 19(c) represent the result of the integral control for the values of $q_1=$

1) Actually x_o7, because of suppressed 2nd order proof mass dynamics.. (Proof mass is clamped on the beam end point during this experiment)
$x_o7=\phi_1(L)x_{o1}+\phi_2(L)x_{o3}+x_{o5}$

1, $q_2=0$, $q_3=1$, $q_4=0.1$, and $R=10^{-5}$. As can be seen in Fig. 19(a), the steady state error of the beam end point is decreased significantly compared to those of Fig. 18(a). The peak values of the end point displacement and velocity are also lowered due to increased control effort of $R=10^{-5}$.

In conclusion, the nonlinearities of the slide base have a degrading effect on the disturbance rejection of the beam end point. The steady state error caused by these nonlinearities is reduced by using integral control.

6.2 Experiment using MMAM and base motor

Both actuators, MMAM and base motor, are used in regulating the end point displacement for

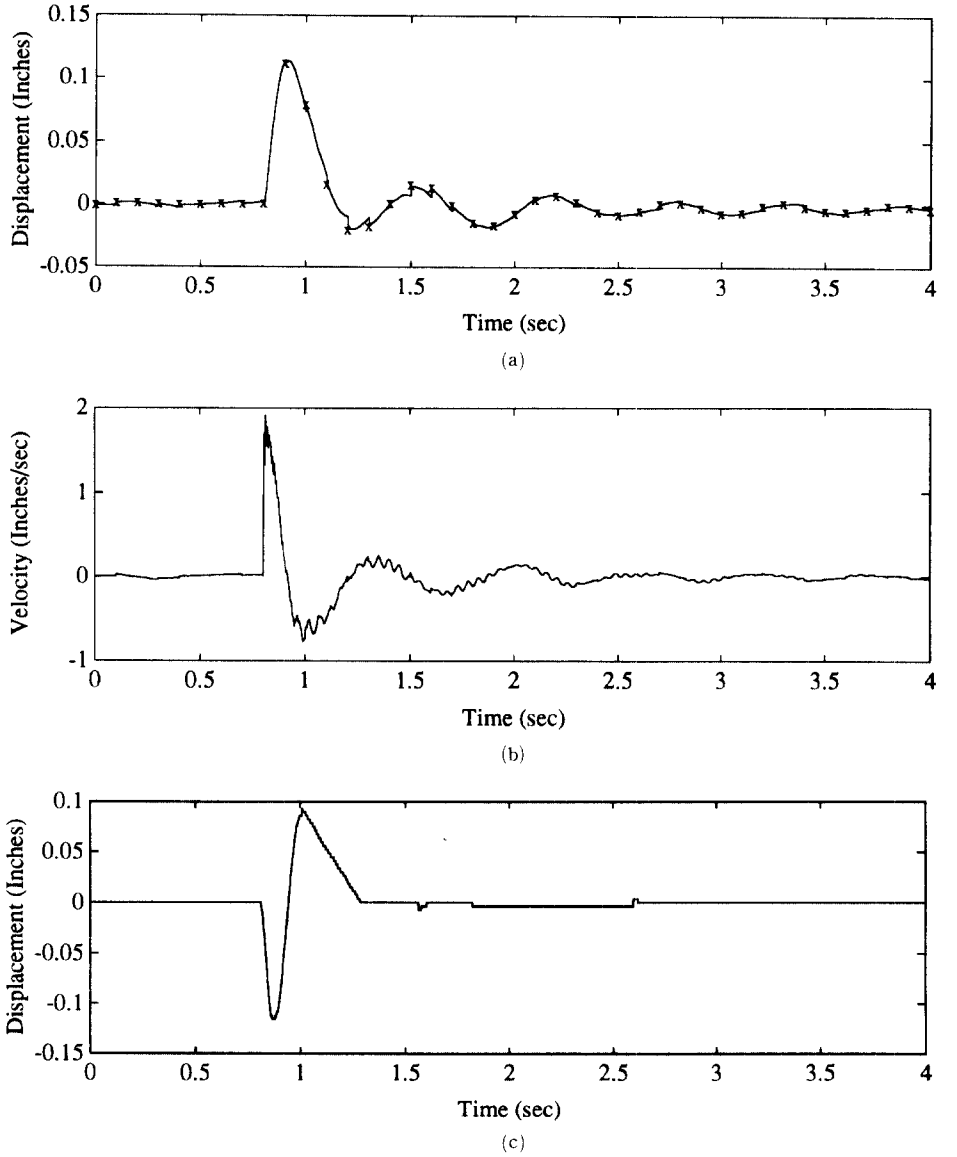

Fig. 19 End point displacement ($q_1=q_3=1$, $q_2=0$, $q_4=0.1$, & R=1.0e-5)
(b) End point velocity ($q_1=q_3=1$, $q_2=0$, $q_4=0.1$, & R=1.0e-5)
(c) Slide base displacement ($q_1=q_3=1$, $q_2=0$, $q_4=0.1$, & R=1.0e-5)

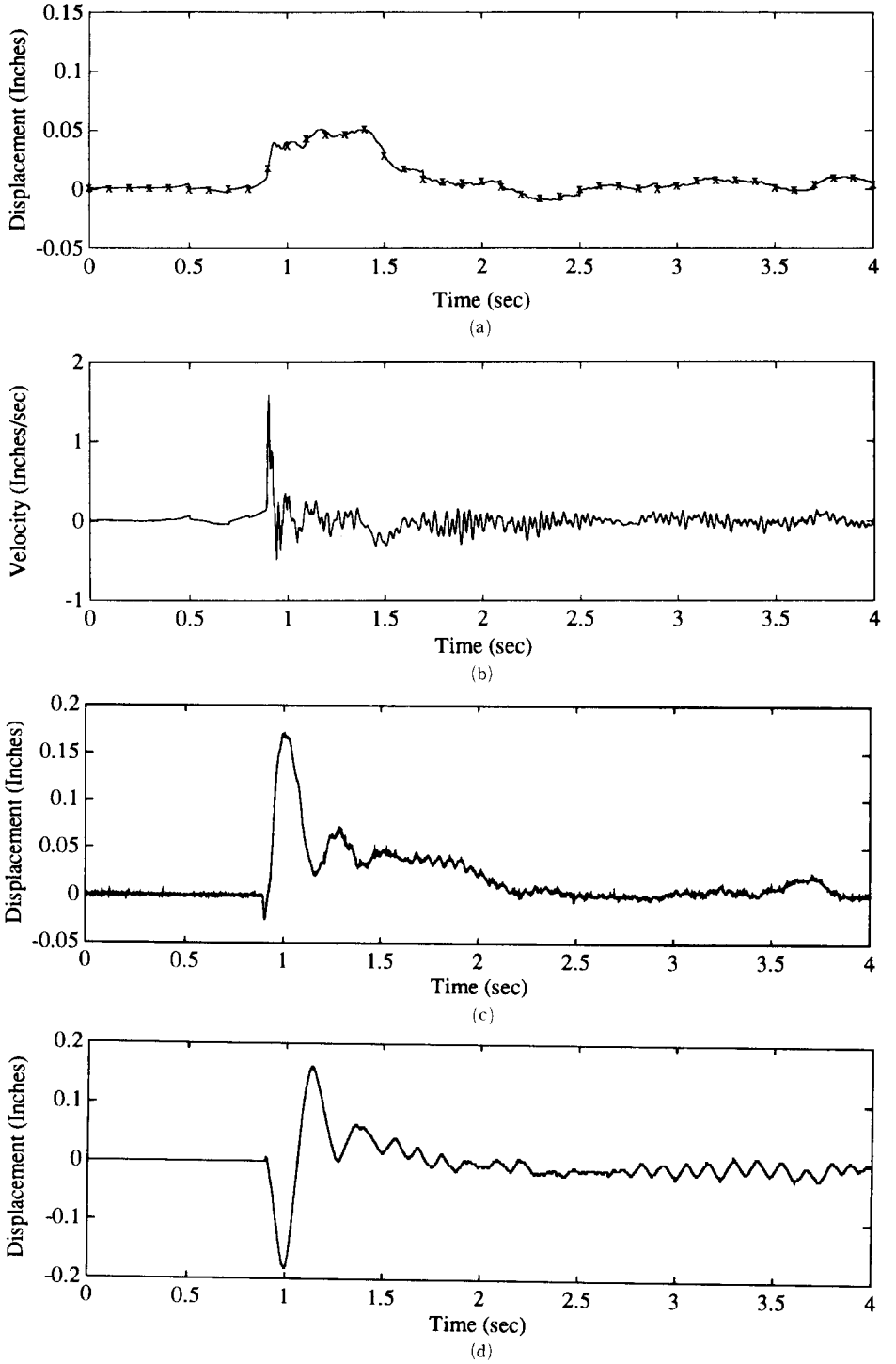

Fig. 20 End point displacement ($q_1=q_2=q_3=1$, $q_4=0.1$, $r_1=30$, & $r_2=0.01$)
(b) End point velocity ($q_1=q_2=q_3=1$, $q_4=0.1$, $r_1=30$, & $r_2=0.01$)
(c) Relative displacement of proof mass ($q_1=q_2=q_3=1$, $q_4=0.1$, $r_1=30$, & $r_2=0.01$)
(d) Slide base displacement ($q_1=q_2=q_3=1$, $q_4=0.1$, $r_1=30$, & $r_2=0.01$)

the same impulse force used in the previous section. The integral control is also applied with the values of $q_1=q_2=q_3=1$, and $q_4=0.1$ in all the experiments listed in this section. Figure 20(a) through Fig. 20(d) show the flexible beam end point displacement, velocity, relative displacement between the beam end point and proof mass, and slide base displacement for $r_1=30$ and $r_2=10^{-2}$. The larger penalty is given to using the MMAM actuator than the slide base DC motor, in order to prevent the proof mass from going away beyond its working range(i.e. ± 0.18 inches). Figure 20(a) displays that the end point displacement seems to be well controlled up to 1 second as expected, but after that it is going away again further from the initial point in spite of the closed loop control action. The reason of this unexpected response is considered as the result of using the term of $q_2(Y-y)^2$ in the performance index of Eq. (33). The inclusion of this term in the cost function means the system is controlled not to allow a large excursion of the proof mass from its neutral position. As shown in Fig. 20(c), the proof mass starts returning to the neutral position after 1 second. This movement of the proof mass results in the opposite force on the beam end point to what should be necessary to regulate the end point displacement to the initial point. But, the proof mass would be out of the working ranges without using the term of $q_2(Y-y)^2$ in the performance index.

As discussed in the above, the small working range of the proof mass is the main obstacle to the high performance control in the disturbance rejection. For the current experimental setup, the performance of disturbance rejection in using both actuators is about 2.5 times better than that of using base motor only (see Figs. 19(a) and 20(a).

7. Conclusion

The concept of MMAM was applied to the end point control of a flexible manipulator. A linear mathematical model is developed for the flexible beam controlled by MMAM actuator and slide base DC motor. A system identification method is applied to estimate some system parameters which can not be measured. To evaluate the accuracy of a model, the frequency response of the beam dynamics has been determined experimentally, and compared with the analytic result. The magnitude of the end point acceleration which can be generated using the MMAM actuator is 10 times larger than that being attained using the movement of the slide base. For an accurate, high bandwidth estimation of the position and velocity of the beam end point, the optimal estimator using combined vision and acceleration measurements has been designed.

For the impulse disturbance at the beam end point, the end point movement is regulated using the optimal linear state feedback control. Integral control is added to decrease the steady state error caused by the nonlinearities of the slide base mechanism such as stiction and dead zone (backlash). The limited working ranges of the proof mass is the main obstacle to the high performance control in the disturbance rejection. For the current experimental setup, the performance of disturbance rejection in using MMAM actuator is about 2.5 times better than that of using base motor only.

References

Albert, T., 1986, "Augmenting the Control of a Flexible Manipulator with Passive Mechanical Damping," Ph. D. Thesis Georgia Tech., Mechanical Eng., Sept.

Book, W.J., Le, S. and Sangveraphunsiri, V., 1984, "Bracing Strategy for Robot Motion," Proc. of RoManSy 84 : the 5th CISM-IFTOMM Symp. on Theory and Practice of Robots and Manipulator, Udine, Italy, June, pp. 179~185.

Cannon Jr., R.H. and Schmitz, E., 1984, "Initial Experiments on the End Point Control of a Flxeible One Link Robot," Int. J. Robotic Research, 3(3), pp. 62~75.

Dickerson, S.L. and Nam, Y.S., 1988 "Milling with Compliant Machine," 1988 USA-Japan Symposium of Flexible Automation, July.

Gelb, A., 1974, "Applied Optimal Estimation," The M.I.T. Press.

Ham, F.M. and Greeley, S.W., 1987, "Active Damping Control Design for the Mast Flight System," Proc. American Control Conference Vol. 1, pp. 355~367.

Hasting, G.G. and Book, W.J., 1985, "Experiments in Optimal Control of a Flexible Arm," Proc. 1985 American Control Conference June, pp. 728~729.

Hollis, R. L., 1987, "A Six Degree of Freedom Magnetically Levitated Variable Compliance Fine Motion Wrist," 4th Int. Symposium for Robotic Research, Santa Kruz, CA, August 8-14.

Kanoh, H. and Lee, H.G., 1985, 1985, "Vibration Control of One Link Flexible Arm," Proc. 24th Conference on Decision and Control, Ft. Laderdale, Fl, Dec. pp. 1172~117.

Lee, E.H and Dickerson, S.L., 1990, "Pinhole Imaging for Industrial Vision System," Symposium on Monitoring and Control for Manufacturing Processing, ASME WAM.

Ljung, L., 1987, "System Identification : Theory for the User," Prentice-Hall.

Meirovitch, L., 1986, "Elements of Vibration Analysis," McGrow-Hill Book Company.

Nam, Y.S., 1991, "Momentum Management for the End Point Control of a Flexible Manipulator," Ph. D. Thesis, Georgia Tech., Mechanical Eng.

Sharon, A. and Hardt, D., 1984, "Enhancement of Robot Accuracy Using End Point Feedback and a Macro-Micro Manipulator System," American Control Conference Proc., San Diago, CA, June 6-8, pp. 1836~184.